Mon. Not. R. Astron. Soc. **370,** 1991–2003 (2006) doi:10.1111/j.1365-2966.2006.10624.x

[Ti II] and [Ni II] emission from the strontium filament of η Carinae

M. A. Bautista,[1⋆] H. Hartman,[2] T. R. Gull,[3] N. Smith[4] and K. Lodders[5]

[1]*Centro de Física, IVIC, PO Box 21827, Caracas 1020A, Venezuela*
[2]*Lund Observatory, Lund University, Box 43, SE-22100 Lund, Sweden*
[3]*Code 667, NASA Goddard Space Flight Center, Greenbelt, MD, USA*
[4]*Center for Astrophysics and Space Astronomy, University of Colorado, 389 UCB, Boulder, CO 80309, USA*
[5]*Planetary Chemistry Laboratory, Department of Earth and Planetary Sciences, Washington University, St. Louis, MO 63130, USA*

Accepted 2006 May 26. Received 2006 May 25; in original form 2006 January 13

ABSTRACT

We study the nature of the [Ti II] and [Ni II] emission from the so-called strontium filament found in the ejecta of η Carinae. To this purpose, we employ multilevel models of the Ti II and Ni II systems, which are used to investigate the physical condition of the filament and the excitation mechanisms of the observed lines. For the Ti II ion, for which no atomic data were previously available, we carry out *ab initio* calculations of radiative transition rates and electron impact excitation rate coefficients. It is found that the observed spectrum is consistent with the lines being excited in a mostly neutral region with an electron density of the order of 10^7 cm^{-3} and a temperature around 6000 K. In analysing three observations with different slit orientations recorded between 2000 March and 2001 November, we find line ratios that change among various observations, in a way consistent with changes of up to an order of magnitude in the strength of the continuum radiation field. These changes result from different samplings of the extended filament due to the different slit orientations used for each observation, and yield clues on the spatial extent and optical depth of the filament. The observed emission indicates a large Ti/Ni abundance ratio relative to solar abundances. It is suggested that the observed high Ti/Ni ratio in gas is caused by dust–gas fractionation processes and does not reflect the absolute Ti/Ni ratio in the ejecta of η Carinae. We study the condensation chemistry of Ti, Ni and Fe within the filament and suggest that the observed gas phase overabundance of Ti is likely the result of selective photoevaporation of Ti-bearing grains. Some mechanisms for such a scenario are proposed.

Key words: atomic data – atomic processes – line: formation – stars: abundances.

1 INTRODUCTION

η Carinae is the most luminous star in our part of the Galaxy and is indeed one of the most mysterious known to us (Davidson & Humphreys 1997). It is surrounded by complex ejecta created in several outbursts of the star and an outgoing massive wind with periodic events every 5.54 yr (Damineli 1996). The largest mass ejection occurred during the so-called Great Eruption observed in the 1840s – which the star survived. In that event, η Carinae released about $10^{49.6}$ erg of kinetic energy contained in more than 10 $M_\odot$ of material (Smith et al. 2003), which has since expanded to form the bipolar Homunculus nebula we see today (Gaviola 1950; Smith & Gehrz 1998; Morse et al. 2001). Despite the hot and very luminous central star, the circumstellar nebula is cool enough to produce a remarkably rich emission spectrum of lines from neutral and low-ionization species like Fe^+ and Ni^+ (Davidson et al. 2001; Zethson 2001; Zethson et al. 2001), line-of-sight absorption from several neutral and singly ionized atoms (Gull et al. 2005), and even emission from H_2 and very cool dust (Smith 2002a; Smith et al. 2003). In addition to being dense and cool, the ejecta of η Carinae are nitrogen rich, representing ashes of the carbon–nitrogen–oxygen (CNO) cycle (Davidson, Walborn & Gull 1982; Davidson et al. 1986; Smith & Morse 2004; Verner, Bruthweiler & Gull 2005). It is the high density, low excitation and CNO abundances of the ejecta that make the Homunculus a unique laboratory among circumstellar nebulae, having a profound effect on the results discussed in this paper.

In 1999 February, a series of Space Telescope Imaging Spectrograph (STIS) observations of η Carinae was made of a region about 1.5 arcsec north-west of the star (Zethson et al. 2001). The spectrum from this region was significantly different from the nebular emission spectra elsewhere in the Homunculus, with two of the lines being identified as forbidden emission of singly ionized strontium ([Sr II]). The measured velocity of the filament (~ -100 km s^{-1}) and its distance from the central star are consistent with the gas having been ejected from the same star during the Great Eruption.

⋆E-mail: bautista@kant.ivic.ve (MAB)

Further spectroscopic observations and a complete list of lines identified in the filament were reported by Hartman et al. (2004). They show that lines of Fe I, V II and Ti II are strong in the filament, whereas only a few Fe II lines are detected. Other lines in the spectrum at about the same velocity come from C I, Mg I, Al II, Ca I, Ca II, Sc II, Cr II, Mn II, Co II and Ni II. Curiously, no H, He, S, O or N lines are present in this region.

The cosmic abundance of strontium is lower than that of iron and nickel by factors of 30 000 and 3000, respectively. Thus, strontium emission is normally undetectable in nebular spectra. The fact that [Sr II] emission was detected with strengths comparable to those of [Fe II] and [Ni II] lines indicates that either strontium is locally overabundant in η Carinae by orders of magnitude, which is inconsistent with the evidence of CNO-cycle-processed ejecta, or very unusual conditions exist in this region of the nebula.

In a recent study of the Sr II and [Sr II] spectra of the filament (Bautista et al. 2002), we found that [Sr II] emission may be strongly enhanced by continuum fluorescence, which partially explains the strength of these lines. Although it was not possible at that time to establish the precise abundance of Sr, this result did imply that Sr might not be as overabundant as previously thought. This point opened up new questions. If [Sr II] lines can be efficiently excited by fluorescence, why are the lines seen only in this structure, but not elsewhere in the Homunculus, and not in any other emission line nebulae?

The observed spatial and velocity distribution of the Sr-filament suggests that it is located in the equatorial region between the hourglass-shaped bipolar Homunculus (Davidson et al. 2001; Smith 2002a; Ishibashi et al. 2003). The Sr-filament is located at a projected distance of 10 lightdays (at 2300 pc distance), where it should receive intense ultraviolet (UV) radiation from η Carinae. The spectra of the Weigelt Blobs B and D, located a few light days from η Carinae, require the spectral flux distribution of an O star with T_e = 35 000 K during the 5-yr broad maximum (Verner et al. 2005). The Sr-filament should receive a diluted amount of this same UV radiation, but its emission-line spectrum indicates a much lower ionization condition. The Sr-filament appears to be shielded not only by neutral hydrogen (13.6 eV), but also by singly ionized iron (7.9 eV) which requires a substantial column density of Fe II between η Carinae and the Sr-filament. One possibility is that the Sr-filament is located at the outer side of an apparent optically thick, dusty, torus seen in the mid-infrared (IR) (Smith et al. 2003). In order to demonstrate this scenario, we must determine the nature of a hot star continuum filtered out by an Fe II blocking column and predict the physical conditions within the filament that would sustain such a low-ionization region. Then, we can determine the actual abundances of all species observed in this structure.

In this paper, we study the emission spectra of two prominent ions in the filament: Ti II and Ni II. Ti II is studied for the very first time as the relevant atomic data have never before been obtained. Ti II emission lines are rarely seen in emission nebulae as its ionization potential, 13.58 eV, leads to Ti III in most H II regions. Ni II, often seen in nebular emission spectroscopy, is much better understood and herein serves as a reference ion.

The remainder of this paper is organized as follows. In Section 2, we present the atomic models built for the Ni II and Ti II systems, with particular detail in the calculations of atomic parameters that had to be performed for Ti II. In Section 3, we show the results of the nebular diagnostics. In Section 4, we derive the relative abundances of Ti II and Ni II in gas phase, while in Section 5 we discuss possible scenarios of Ni and Ti depletion in the nebula. Finally, our discussion and conclusions are given in Section 6.

2 ATOMIC DATA AND ATOMIC MODELS FOR NI II AND TI II

For the present analysis of [Ni II] spectra, we employ a 76-level model for the ion that includes continuum fluorescence excitation as in Bautista, Peng & Pradhan (1996) and improved collisional data reported by Bautista (2004). This new collisional data, that results from very extensive calculations, are expected to be more accurate than previous data.

2.1 Radiative data for Ti II

For Ti II, neither complete transitions rates for forbidden transitions nor collision strengths had been reported; thus large calculations of atomic data for this ion were carried out within the present work.

For the calculation of radiative transition probabilities and for the wavefunctions of the Ti II system, we use the atomic structure code AUTOSTRUCTURE (Badnell 1986) to reproduce the structure of the ion. This code is based on the program SUPERSTRUCTURE originally developed by Eissner, Jones & Nussbaumer (1974). In this approach, the wavefunctions are written as a configuration interaction expansion of the type

$$\psi_i = \sum_j \phi_j c_{ji}, \tag{1}$$

where the coefficients c_{ji} are chosen so as to diagonalize $\langle \psi_i \, |H| \, \psi_j \rangle$, where H is the Hamiltonian and the basic functions ϕ_j are constructed from one-electron orbitals generated using the Thomas–Fermi–Dirac model potential (Eissner & Nussbaumer 1969). The λ_{nl} scaling parameters in this model are optimized by minimizing a weighted sum of energies. Representing a system as complex as Ti II requires many configurations, which must be selected rather carefully as to account for all strongly coupled configurations without exceeding available computational resources. Experience shows that configurations with one and two electron promotions out of the 3s, 3p and 3d orbitals are often important. Further, improvements can be obtained in some cases through the use high laying non-physical orbitals. For the present Ti II model, it was necessary to include several non-physical orbitals in the expansion, i.e. $\bar{4}$d, $\bar{5}$d, $\bar{5}$s, $\bar{5}$p, $\bar{4}$f. The configuration representation and scaling parameters used in this work are listed in Table 1.

Fine-tuning (semi-empirical corrections) – which is useful for treating states that decay through weak relativistic couplings (e.g. intercombination transitions) – takes the form of term energy

Table 1. Ti II configurations and scaling parameters.

Spectroscopic configurations
$3\,s^2\,3\,p^6\,3\,d^3$, $3\,s^2\,3\,p^6\,3\,d^2\,4\,s$, $3\,s^2\,3\,p^6\,3\,d^2\,4\,p$, $3\,s^2\,3\,p^6\,3\,d\,4\,s^2$
Correlation configurations
$3s^2\,3p^6\,3d^2\,\bar{4}d$, $3s^2\,3p^6\,3d\,4s\,4p$, $3s^2\,3p^6\,3d\,4s\,\bar{4}d$,
$3s^2\,3p^6\,3d\,4s\,\bar{5}s$, $3s^2\,3p^6\,3d\,4s\,\bar{5}d$, $3s^2\,3p^6\,3d\,4s\,\bar{5}p$,
$3s^2\,3p^6\,3d\,4s\,\bar{4}f$, $3s^2\,3p^6\,3d\,4p^2$, $3s^2 3p^5\,3d^4$, $3s^2\,3p^5\,3d^3\,4s$,
$3\,s^2\,3\,p^5\,3\,d^3\,4\,p$, $3\,s^2\,3\,p^5\,3\,d^2\,4\,s^2$, $3\,s^2\,3\,p^4\,3\,d^5$, $3\,s^2\,3\,p^4\,3\,d^3\,4\,s^2$
$3\,s^2\,3\,p^4\,3\,d^4\,4\,s$, $3\,s^2\,3\,p^4\,3\,d^4\,4\,p$, $3\,s\,3\,p^6\,3\,d^4$, $3\,s\,3\,p^6\,3\,d^3\,4\,s$,
$3\,s\,3\,p^6\,3\,d^3\,4\,p$ $3\,s\,3\,p^5\,3\,d^4\,4\,s$, $3\,s\,3\,p^5\,3\,d^4\,4\,p$, $3\,p^6\,3\,d^4\,4\,s$,
$3\,p^6\,3\,d^4\,4\,p$
λ_{nl}
1.43570(1s), 1.12290(2s), 1.06650(2p), 1.09690(3s), 1.08430(3p),
1.12590(3d), 1.27470(4s), 1.22660(4p), −0.79940($\bar{4}$d)
−0.64020($\bar{5}$s), 2.99520($\bar{5}$d), 1.90030($\bar{5}$p), 1.88930($\bar{4}$f)

Table 2. Energy terms in Rydberg for the Ti II ion relative to the ground state. The table compares experimental energies with *ab initio* calculated energies (Theo.) and energies with term energy corrections (Theo.-TEC).

	Config.	Term	Theo.	Theo.-TEC	Exp.
1	$3d^2(^3F)4s$	$a\ ^4F$	0.0	0.00	0.0
2	$3d^3$	$b\ ^4F$	0.08806	0.00834	0.007839
3	$3d^2(^3F)4s$	$a\ ^2F$	0.06439	0.04231	0.041528
4	$3d^2(^1D)4s$	$a\ ^2D$	0.08922	0.05534	0.077508
5	$3d^3$	$a\ ^2G$	0.09982	0.08140	0.080552
6	$3d^3$	$a\ ^4P$	0.09202	0.08543	0.084077
7	$3d^3$	$a\ ^2P$	0.09217	0.07588	0.088476
8	$3d^2(^3P)4\ s$	$b\ ^4P$	0.10519	0.09021	0.088784
9	$3d^3$	$b\ ^2D$	0.13436	0.11686	0.113737
10	$3d^3$	$a\ ^2H$	0.14976	0.11788	0.113935
11	$3d^2(^1G)4s$	$b\ ^2G$	0.18304	0.14025	0.137017
12	$3d^2(^3P)4s$	$b\ ^2P$	0.19358	0.16370	0.149115
13	$3d^3$	$b\ ^2F$	0.22551	0.19290	0.188561
14	$3d\ 4\ s^2$	$c\ ^2D$	0.37419	0.20894	0.226677
15	$3d^2(^3F)4p$	$z\ ^4G^o$	0.24771	0.26968	0.270750
16	$3d^2(^3F)4p$	$z\ ^4F^o$	0.25782	0.28059	0.281422
17	$3d^2(^3F)4p$	$z\ ^2F^o$	0.26630	0.27996	0.285498
19	$3d^2(^1S)4s$	$a\ ^2S$	0.35738	0.28071	0.287619
18	$3d^2(^3F)4p$	$z\ ^2D^o$	0.27074	0.29066	0.288805
20	$3d^3$	$d\ ^2D1$	0.28882	0.34006	0.292376
21	$3d^2(^3F)4p$	$z\ ^4D^o$	0.27443	0.29206	0.295841
22	$3d^2(^3F)4p$	$z\ ^2G^o$	0.30665	0.31108	0.313768
23	$3d^2(^3P)4p$	$z\ ^2S^o$	0.32376	0.33886	0.339041
24	$3d^2(^1D)4p$	$z\ ^2P^o$	0.34940	0.35509	0.356748
25	$3d^2(^1D)4p$	$y\ ^2D^o$	0.35800	0.35671	0.358146
26	$3d^2(^1D)4p$	$y\ ^2F^o$	0.35890	0.35852	0.362557
27	$3d^2(^3P)4p$	$z\ ^4S^o$	0.35195	0.36370	0.362702
28	$3d^2(^3P)4p$	$y\ ^4D^o$	0.36084	0.36767	0.368031
29	$3d^2(^3P)4p$	$z\ ^4P^o$	0.37814	0.38047	0.381834
30	$3d^2(^1G)4p$	$y\ ^2G^o$	0.40620	0.39781	0.396745
31	$3d^2(^3P)4p$	$x\ ^2D^o$	0.41916	0.41092	0.407173
32	$3d^2(^3P)4p$	$y\ ^2P^o$	0.42858	0.40434	0.412787
33	$3d^2(^1G)4p$	$z\ ^2H^o$	0.43455	0.41952	0.415324
34	$3d^2(^1G)4p$	$x\ ^2F^o$	0.45445	0.43599	0.431113
35	$3d^2(^1S)4p$	$^2P^o$	0.61270	0.57783	0.569851

corrections (TEC). By considering the relativistic wavefuntion, $\psi_i^{\rm r}$, in a perturbation expansion of the non-relativistic functions $\psi_i^{\rm nr}$,

$$\psi_i^{\rm r} = \psi_i^{\rm nr} + \sum_{j\neq i} \psi_j^{\rm nr} \times \frac{\left\langle \psi_j^{\rm nr} \middle| H_{\rm 1b} + H_{\rm 2b} \middle| \psi_i^{\rm nr} \right\rangle}{E_i^{\rm nr} - E_j^{\rm nr}}, \qquad (2)$$

where $H_{\rm 1b}$ and $H_{\rm 2b}$ are the one- and two-body Breit–Pauli relativistic operators. Thus, a modified $H_{\rm nr}$ is constructed with improved estimates of the differences $E_i^{\rm nr} - E_j^{\rm nr}$ so as to adjust the centres of gravity of the spectroscopic terms to the experimental values. Table 2 shows a comparison between the observed energies averaged over the fine structure taken from Huldt et al. (1982), Moore (1949) and Russell (1927) and compiled in the National Institute of Standards and Technology (NIST) energy levels data base (NIST 2000), the computed *ab initio* term energies and the computed energies after TEC corrections. The overall agreement between *ab initio* energies and experimental values is typically within 10 per cent, with better agreement for the odd parity terms but with some problems for low laying even parity multiplets. To the limit of our computations, we were unable to find a set of correlation configurations able to reproduce *ab initio* the correct order of the terms $3d^3\ a\ ^2G$, $a\ ^4P$ and $a^2\ P$ (terms 5 through 7). We also found it difficult to reproduce the position and an accurate energy for the $3d4s^2\ c\ ^2D$ term. These large discrepancies between calculated and experimental energies were readily resolved by the TEC technique, although some corrections were uncomfortably large. A notable exception is the $a\ ^2D$ term, which lowers its energy far from the experimental value after TEC corrections. This term could not be improved further as it has a profound effect on the perturbative corrections on the b^4 F and a^2 F terms.

Table 3. Comparison between $\log(gf)$-values for dipole-allowed transitions from the present work, and those of Pickering et al. (2001, 2002), Bizzarri et al. (1993), Kurucz (2000) and the values recommended by NIST.

Wave (nm)	Present	Pickering	Bizzarri	Kurucz	NIST
Upper level: 29 544 cm^{-1} $3d^2(^3F)4p\ z\ ^4G_{5/2}$					
401.23835	−1.14	−1.84	−1.75	−1.73	−1.61
349.10494	−1.01	−1.15	−1.06	−1.13	
340.98043	−1.80	−1.98	−1.89	−1.89	−1.90
339.45720	−0.56	−0.55	−0.54	−0.52	−0.59
338.37587	−0.052	0.16	0.15	0.20	0.050
Upper level: 31490 cm^{-1} $3d^2(^3F)4p\ z\ ^2F_{7/2}$					
465.72004	−2.68	−1.59	−1.63	−1.59	−2.15
439.50311	−0.92	−0.54	−0.51	−0.45	−0.66
375.92914	0.16	0.28	0.27	0.31	0.20
321.47669	−3.30	−1.40	−1.34	−1.35	−1.39
319.75185	−0.30	−1.97	−1.90	−2.55	−1.87
1587.3644	−1.38			−1.92	

This ion's representation was used to compute radiative transition rates for both dipole-allowed and forbidden transitions. Table 3 shows a comparison between the present $\log(gf)$-values for dipole-allowed transitions and those determined experimentally by Pickering, Thorne & Perez (2001, 2002) and Bizzarri et al. (1993), computed by Kurucz (2000), and those compiled in the NIST data base (taken from Roberts, Andersen & Sorensen 1973; Meggers, Corliss & Scribner 1975; Roberts, Voigt & Czernichowski 1975; Danzmann & Kock 1980; Blackwell, Menon & Petford 1982). Most gf-values in the NIST data base have an accuracy rating 'D', which means that the uncertainties are greater than 50 per cent. Table 3 is limited to lines with gf-values greater than 0.01 for which reasonably accurate data are expected given the present representation of the ion. We find good agreement, within 0.2 dex, between our results and those of other authors for $\log(gf) > -1$ and a mean dispersion of about 0.5 dex for smaller values. Given the uncertainties in the present results, for our Ti II multilevel model we combine the NIST f-values whenever available with the present radiative data for all other transitions.

Our representation of the ion was also used to compute electric quadrupole and magnetic dipole transition rates. The results of such calculations are rather sensitive to configuration interactions and level mixing. Some indication about the accuracy of the present rates is obtained from recent measurements by the FERRUM project (Hartman et al. 2003, 2005) of lifetimes of metastable levels, which decay through parity forbidden transitions. Lifetimes for five levels have been reported so far, which are compared in Table 4 with our theoretical results. Our calculated lifetimes agree within ∼50 per cent with the experimental determinations, which is the estimated overall uncertainties for the present radiative rates for forbidden transitions.

Table 4. Lifetimes (in s) for metastable levels of Ti II as determined experimentally by Hartman et al. (2003, 2005) and from the present calculations.

Level	Hartman	Present
$3d^2(^3P)4s\,b\,^4P_{3/2}$	18(4)	31.1
$3d^2(^3P)4s\,b\,^4P_{5/2}$	28(10)	16.4
$3d^2(^3P)4s\,b\,^2P_{1/2}$	14(3)	12.7
$3d4s^2\ \ c\,^2D_{3/2}$	0.29(0.01)	0.192
$3d4s^2\ \ c\,^2D_{5/2}$	0.33(0.02)	0.196

2.2 Collisional data for Ti II

We have computed electron impact collision strengths for transitions among the lowest 82 energy levels of Ti II that belong to the configurations $3d^3$, $3d^24s$, $3d^24p$ and $3d4s^2$. We employ the Breit–Pauli R-matrix method and the BPRM set of codes developed in the framework of the IRON Project (Hummer et al. 1993; Berrington et al. 1995). Partial wave contributions are included from 60 $SL\pi$ total symmetries with angular momentum $L = 0 - 9$, total multiplicities $(2S + 1) =$ 1–5 and parities even and odd. Then, the collision strengths were 'topped up' with estimates of contributions from higher partial waves based on the Coulomb–Bethe approximation (Burgess 1974). Collision strengths for the fine-structure levels were obtained by algebraic recoupling of the LS reactance matrices (Hummer et al. 1993). The collision strengths were calculated at 11 000 energy points from 0 to 6 Ry, with 90 per cent of the points in the region with resonances. This number of energy points was found to provide sufficiently good resolution for accurate calculations of the contributions of autoionizing resonances to the effective collision strengths at temperatures between 5000 and 20 000 K. Fig. 1 shows the collision strengths for some of the dominant transitions.

We compute Maxwellian-averaged effective collision strengths, defined as

$$\Upsilon(T) = \int_0^\infty \Omega_{if}(\epsilon_f)\exp(-\epsilon_f/kT)\,\mathrm{d}(\epsilon_f/kT), \qquad (3)$$

where Ω_{if} is the collision strength for the transition i to f, and ϵ_f is the energy of the outgoing electron. The Υs were computed for various temperatures between 5000 and 20 000 K to be used in the calculation of excitation rates.

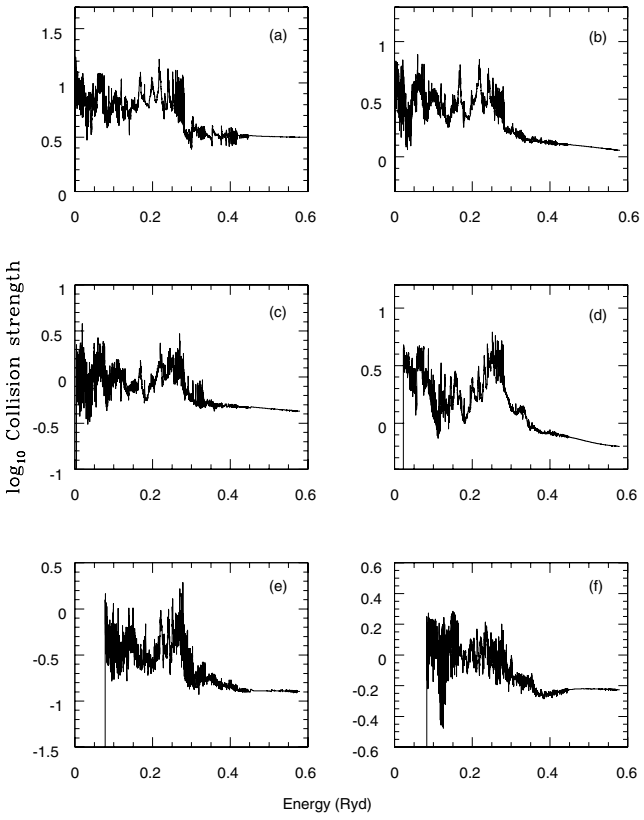

Figure 1. Collision strengths versus incident electron energy for excitations from the ground level $a\ ^4F_{3/2}$ to $a\ ^4F_{5/2}$ (a), $a\ ^4F_{7/2}$ (b), $a\ ^4F_{9/2}$ (c), $b\ ^4F_{3/2}$ (d), $a\ ^2F_{7/2}$ (e), $a\ ^2D_{3/2}$ (f).

2.3 Multilevel model of Ti II

We built an 82-level excitation equilibrium model for Ti II which considers both electron impact excitation and continuum fluorescence excitation. A model of this size is large enough to account for collisionally excited emission at the temperatures of interest ($\sim 10^4$ K), and the dominant photoexcitation channels from the ground level. If more levels were included in our models, they would tend to increase the efficiency of continuum fluorescence excitation, although it has been shown that the contribution of individual levels decreases rapidly with the level energy (Bautista et al. 1996). We assume that the radiation field density, U_ν, at photon energies below the Lyman ionization limit (13.6 eV) can be approximated by a blackbody with temperature T_R times a geometrical dilution factor w, i.e.

$$\frac{c^3U_\nu}{8\pi h\nu^3} = \frac{w}{\exp(h\nu/kT_R) - 1}.$$

For the present calculations, we adopt a blackbody temperature of 35 000 K (see Verner et al. 2005) while the dilution factor is diagnosed from the observed spectra. A different choice in the blackbody temperature would lead to a change in the diagnosed dilution factor, but would have negligible effect on the modelled spectrum.

Fig. 2 presents a diagram of the dominant photoexcitation channels for two [Ti II] lines arising from quartets and doublets terms. The main photoexcitation channels are indicated by dashed lines, and the radiative deexcitation transitions are marked by solid lines. Such dipole-allowed radiative decays lead to emission lines, observable in the spectra, just as they populate the levels that give rise to forbidden lines. It is worth noting that in the absence of collisional excitation, the strength of forbidden lines would be tightly bound to the intensity of the dipole transitions from the pumping mechanism. On the other hand, the contribution of collisional excitations to the forbidden lines introduces a complex temperature and density dependence in the relative strengths of dipole and forbidden transitions, which can be used for spectral diagnostics as illustrated in the next section.

Fig. 3 presents the line emissivity per ion of the Ti II lines [λ6648] ($b\ ^2G_{7/2} - a\ ^4F_{7/2}$) and [$\lambda$4918] ($c\ ^2D_{3/2} - a\ ^2F_{5/2}$) and the blend [$\lambda$10069$b$] ($b\ ^4P_{3/2} - a\ ^4F_{3/2} + b\ ^4P_{5/2} - a\ ^4F_{5/2}$) versus N_e for an electron temperature of 6000 K, a blackbody temperature of 35 000 K and four values of the dilution factor, w= 0, 10^{-10}, 5×10^{-10} and 10^{-9}. For electron densities less than $N_e \sim 10^7$ cm^{-3}, continuum fluorescence dominates the strength of most lines. On the other hand, for electron densities around $N_e \sim 10^7$, as previously diagnosed for the strontium filament (Bautista et al. 2002), collisional excitation dominates the [λ6648] and [λ10069b] features, while fluorescence still makes a very significant contribution to the excitation of the $c\ ^2D_{3/2}$ level, responsible for the [λ4918] line. This

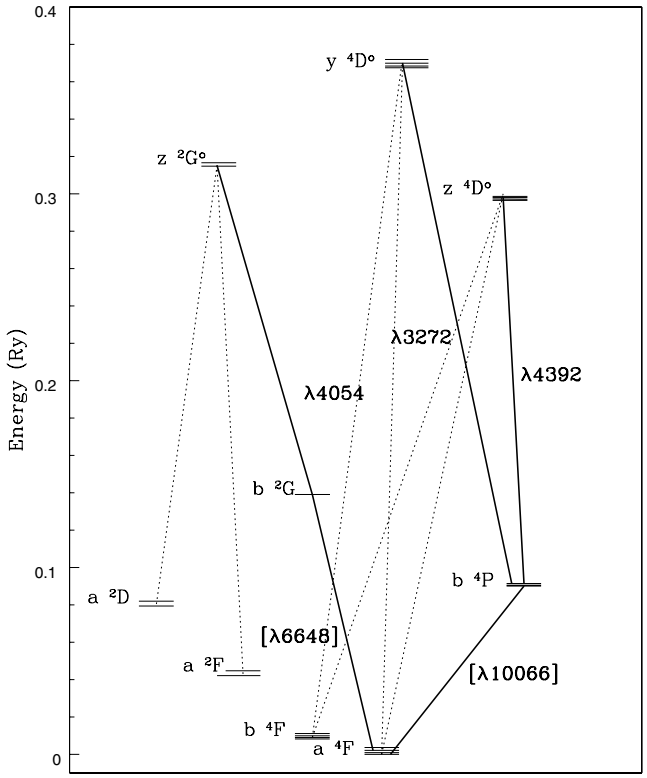

Figure 2. Dominant photoexcitation channels for two [Ti II] lines. Some of the dipole-allowed lines also emitted in the photopumping process are also indicated.

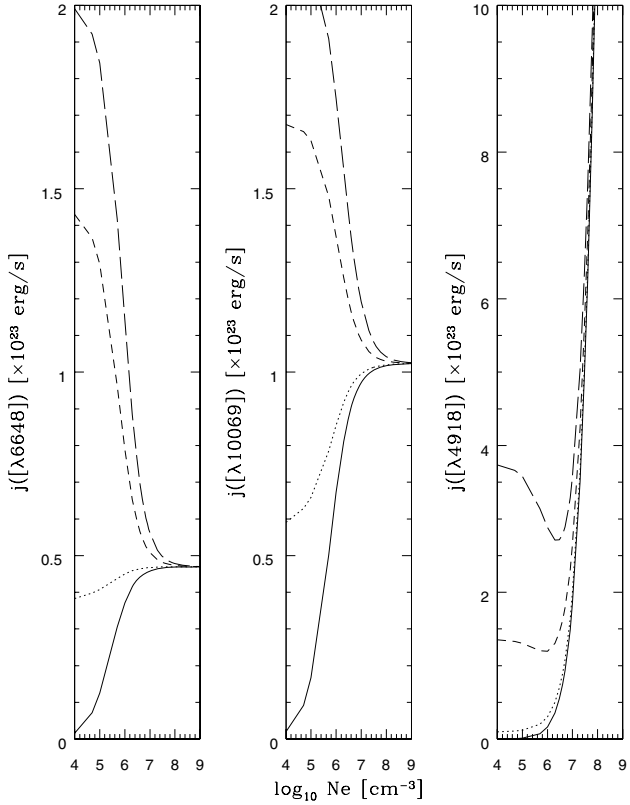

Figure 3. Line emissivity of the [Ti II] λλλ6648, 10069 and 4918 lines ion versus electron density for dilution factors, $w = 0$ (solid line), 10^{-10} (dotted line), 5×10^{-10} (short-dashed line) and 10^{-9} (long-dashed line). The curves are calculated for $T_e = 6000\ K$, $N_e = 10^7\ cm^{-3}$ and a blackbody temperature of 35 000 K.

is because collisional transition rates from the ground levels to the $c\ ^2D$ multiplet are rather small.

3 SPECTRAL DIAGNOSTICS

We use the [Ni II] and [Ti II] emission-line strengths to diagnose the physical conditions of the filament on each of the three *Hubble Space Telescope* (*HST*)/STIS observations: 2000 March, 2001 April and 2001 November (hereafter mar00, apr01 and nov01, respectively; Bautista et al. 2002; Hartman et al. 2004). Previous diagnostics were reported in Bautista et al. (2002) from the [Sr II] lines. There, we estimated an electron density of the order of $10^7\ cm^{-3}$ and an upper limit to the dilution factor for photoexcitation of $\sim 10^{-9}$.

3.1 Observed line intensities

For the present work, we use the deep spectra extending from 1640 to 10 100 Å analysed by Hartman et al. (2004). The original data were recorded during three visits with the *HST*/STIS under several different observational programs. For the mar00 observation, the long 52×0.2 arcsec^2 aperture was aligned close to the axis of the Homunculus [position angle (PA) $-41°$], whereas the aperture was aligned at 22° in apr01 and $-130°$ in nov01. The different angles were defined primarily by *HST* Sun-angle restrictions, but were used to study the extent of the Strontium filament in different directions. The intersection of these apertures (see fig. 1 in Hartman et al. 2004) is on the apparent peak of the Strontium filament as first noted by the discovery observations (Zethson et al. 2001).

The line fluxes were integrated across the line profiles of the components centred at ~ -100 km s^{-1} at specific positions along the slit. The intersection position of the different visits is the primary position of interest. However, as noted below, several additional positions were sampled along the aperture oriented radially to η Carinae (PA $= -41°$) and tangentially ($-130°$) to understand the spatial variation of specific line ratios and therein to study the excitation and ionization structure of the filament. The measured line intensities vary along the aperture and between visits. The structure is complex as other nebular structures are in line of sight: namely the Homunculus and the Little Homunculus. At some positions, Hartman et al. (2004) noted a second velocity structure in many lines. These two velocity systems are likely related to the two discs noted by Davidson et al. (2001) located between the bipolar lobes. The two velocity components correspond to material in the same equatorial disc but with two different ages, as noted by Davidson et al. (2001). The more prominent feature is associated with the parts of the skirt ejected along with the Homunculus in the 1840s. The fainter and more blueshifted feature is also in the equator, but was ejected in the 1890 outburst along with the Little Homunculus (Ishibashi et al. 2003; Smith 2005) and the Weigelt knots (Smith et al. 2004; Weigelt et al. 1995). In this study, we focus on the structure ejected in the 1840s.

As with any spectroscopic analysis, the observed line intensities must be corrected for extinction. None of the lines that form the classical line ratios (e.g. hydrogen recombination lines) is detected. We use two relatively well-known [Ni II] transitions that arise from a common upper level, i.e. λ7413($a\ ^2D_{3/2} - a\ ^2F_{5/2}$) and λ6668 ($a\ ^2D_{5/2} - a\ ^2F_{5/2}$), and the standard interstellar extinction curve of

Cardelli, Clayton & Mathis (1989). While these lines are relatively close in wavelength, thus far they are the best candidates for estimating extinction as all other lines of interest are much weaker or their predicted line ratios are less certain. The observed line ratios are 2.20 ± 0.13 in mar00, 1.94 ± 0.13 in apr01 and 2.07 ± 0.13 in nov01. Thus, there are no significant variations of the line ratio between the three observations. From these observations, we derive an extinction magnitude, $A_V = 2.1 \pm 0.9$, as required to correct the ratios to the theoretical value of 1.6, with an estimated uncertainty of ∼10 per cent. The relatively large uncertainty in A_V comes from the fact that the two lines used in the diagnostic are close in wavelength. This value for the extinction magnitude is consistent with the value measured, $A_V = 2.06$, from photometry of stars of the Tr 16 cluster in the Carinae nebula (Tapia et al. 2003). The actual extinction magnitude to the filament could be somewhat higher than to the Carinae stars due to the dust within the nebula. Smith (2002b) studied local extinction within the larger Carina Nebula, and found a total-to-selective extinction of $R = A_V/E(B-V) = 4.8$, which is different from the normal interstellar medium (ISM) value of 3.1. Furthermore, the extinction around η Carinae itself is likely to be very grey because of the large grain size (Smith et al. 2003). However, thermal-IR maps of the dust column density in the Homunculus reveal a local minimum near the position of the Sr filament (Smith et al. 2003), so the unusual reddening there may not be a severe problem. We thus adopt for the remaining of this paper an extinction law with $A_V = 2.1$ and the interstellar $R = 3.1$. Clearly, the remaining uncertainty on this value can be important in trying to compare lines well separated in wavelength; thus all diagnostics should be carried out with lines close to each other.

Tables 5 and 6 present the complete lists of [Ni II] and [Ti II] lines used for the present study and their intensities corrected for extinction.

3.2 [Ni II] diagnostics

The combined contributions of collisional excitation and fluorescence make spectral diagnostics much more difficult than with traditional collisionally excited lines. Most line ratios of interest become simultaneously sensitive to electron density, temperature and the continuum radiation field (i.e. dilution factor); thus many lines have to be studied as a whole to derive reliable conclusions about the physical conditions of the emitting plasma.

In the case of [Ni II] lines, only a few diagnostic line ratios can be used because out of the seven dipole forbidden lines measured in the spectrum several share the same upper level. Fig. 4 shows the line ratio $I([\lambda\lambda 6668 + 7413])/I([\lambda 7379])$, $I([\lambda\lambda 4327 + 7257])/I([\lambda\ 7379])$ and $I([\lambda\lambda 4327 + 7257])/I([\lambda\lambda\ 6668 + 7413])$ against the logarithm of the dilution factor. The ratios were computed for three values of the electron density, $N_e = 10^6$, 10^7 and 10^8 cm^{-3} displayed in separated panels from left to right in the figure. In each panel, we present the line ratios as computed for temperatures of 5000, 7000 and 9000 K. The observed line ratios are indicated in the plots by horizontal lines for each observation. Two conclusions can be derived from these plots with regard to the dilution factor in the filament. First, for the nov01 observation the value of $\log_{10} w$ is between −9.2 and −8.5. There is evidence for different dilution factors for each of the three observations, with a difference as large as 1 dex between the mar00 and the apr01 observations, with the higher value corresponding to the mar00 observation. The dilution factor from the nov01 observation lies between the values for the other two observations. The spread in line ratios, and consequently on derived physical conditions, in the three observations is the result of different orientations of the spectrograph slit with respect to the star (see Hartman et al. 2004). For the mar00 observations, the slit was centred on η Carinae with the fiducial, F2, blocking the starlight. This provided a spatial sampling of the Sr-emitting region extending radially from the central source. That this spectrum yields the highest value for the dilution factor is due to finding the radial distance for which both apply. The nov01 spectrum was taken at PA −130° and provided a slice of the Sr-filament that is tangential to the distance from the central source. As the position of the slit is more distant than the optimal position for highest dilution factor, we get a lower value for the dilution factor along this slit. The dilution factor changes by an order of magnitude between the optimal radial position and the tangential sample because these observations sample slightly different spatial regions. Photons with energies below 7.9 eV encounter increasing optical depths with distance from the central source. For these energies, the main source of opacity is free–free opacity (bremsstrahlung). Assuming an electron temperature of the order of 10^4 K, density $\sim 10^7$ cm^{-3} and a difference in the path length within the filament between the two observations of ∼0.3 arcsec ≈ 10^{16} cm, one gets an optical depth, $\tau \approx 2$, which is consistent with the observed variation in the dilution factor.

3.3 [Ti II] diagnostics

The large number of Ti II and [Ti II] lines present in the spectra allows us to constrain the physical conditions of the filament.

Table 5. [Ni II] lines from the Sr-filament.

λ_{lab}	Transition	Observed flux (10^{-13} erg s^{-1} cm^{-2} arcsec^{-1})			Extinction corrected flux ($A_V = 2.1$)		
		Mar00	Apr01	Nov01	Mar00	Apr01	Nov01
7379.970	$a\ ^2F_{7/2} - a\ ^2D_{1/2}$	286.00	211.00	239.00	1088.0	802.7	909.2
8303.270	$a\ ^2F_{7/2} - a\ ^2D_{3/2}$			11.80			34.6
6668.670	$a\ ^2F_{5/2} - a\ ^2D_{1/2}$	64.60	41.60	51.30	304.3	195.9	241.6
7413.690	$a\ ^2F_{5/2} - a\ ^2D_{3/2}$	142.0	80.60	106.0	534.8	303.5	399.2
4327.453	$a\ ^4P_{5/2} - a\ ^2D_{1/2}$		18.10	27.00		246.8	368.1
7257.860	$a\ ^4P_{5/2} - a\ ^4F_{7/2}$	23.00	12.80	10.70	90.8	50.5	42.2
6815.450	$a\ ^4P_{3/2} - a\ ^4F_{5/2}$	15.00	5.71	7.32	67.6	25.7	33.0
6793.350	$a\ ^4P_{1/2} - a\ ^4F_{5/2}$	10.40	3.50	19.70	47.2	15.9	89.4

Table 6. [Ti II] lines from the Sr-filament.

λ_{lab}	Transition	Observed flux (10^{-13} erg s^{-1} cm^{-2} arcsec^{-1})			Extinction corrected flux ($A_V = 2.1$)		
		Mar00	Apr01	Nov01	Mar00	Apr01	Nov01
4918.247	$c\ ^2D_{3/2} - a\ ^2F_{5/2}$	13.60	8.62	11.50	124.8	61.5	105.6
4984.205	$c\ ^2D_{3/2} - a\ ^2F_{7/2}$	2.64	1.32	2.00	23.3	11.7	17.7
6153.623	$c\ ^2D_{3/2} - a\ ^2D_{3/2}$			3.76			24.0
4927.288	$c\ ^2D_{5/2} - a\ ^2F_{7/2}$	14.70	13.2b	13.40	134.2	120.5	122.4
6079.567	$c\ ^2D_{5/2} - a\ ^2D_{5/2}$			2.86			16.1
6126.311	$b\ ^2F_{5/2} - a\ ^2F_{5/2}$			11.8			65.5
6228.990	$b\ ^2F_{5/2} - a\ ^2F_{7/2}$			2.03			10.9
6148.896	$b\ ^2F_{7/2} - a\ ^2F_{5/2}$			3.20			17.6
6252.341	$b\ ^2F_{7/2} - a\ ^2F_{7/2}$			18.8			100.3
6652.610	$b\ ^2G_{9/2} - a\ ^4F_{7/2}$	3.36	1.97	2.32	15.9	9.3	11.0
6727.670	$b\ ^2G_{9/2} - a\ ^4F_{9/2}$	5.12	4.78	5.38	23.7	22.1	24.9
9652.716	$b\ ^2G_{9/2} - a\ ^2F_{7/2}$	0.71		1.39	1.7		3.3
9408.356	$b\ ^2G_{9/2} - a\ ^2F_{5/2}$	2.62		1.58	6.3		3.8
6648.980	$b\ ^2G_{7/2} - a\ ^4F_{7/2}$	1.87	1.67	1.42	8.9	7.9	6.7
9645.089	$b\ ^2G_{7/2} - a\ ^2F_{7/2}$	1.02		0.60	2.4		1.4
7918.452	$b\ ^2D_{3/2} - a\ ^4F_{3/2}$			2.62			8.5
7977.897	$b\ ^2D_{3/2} - a\ ^4F_{5/2}$			6.03b			19.3
8531.906	$b\ ^2D_{3/2} - b\ ^4F_{3/2}$			11.00			30.5
8587.494	$b\ ^2D_{3/2} - b\ ^4F_{5/2}$			5.78			15.8
8664.452	$b\ ^2D_{3/2} - b\ ^4F_{7/2}$			53.8b			
7979.330	$b\ ^2D_{5/2} - a\ ^4F_{7/2}$			6.03b			
8568.400	$b\ ^2D_{5/2} - b\ ^4F_{7/2}$			6.44			17.7
8663.807	$b\ ^2D_{5/2} - b\ ^4F_{9/2}$			53.80b			150.2
8335.590	$b\ ^2P_{3/2} - a\ ^2F_{5/2}$			3.74			10.9
8526.997	$b\ ^2P_{3/2} - a\ ^2F_{7/2}$			13.90			38.6
8412.354	$b\ ^2P_{1/2} - a\ ^2F_{5/2}$			7.72			22.0
10069.74b	$b\ ^4P_{5/2} - a\ ^4F_{5/2}$ $b\ ^4P_{3/2} - a\ ^4F_{3/2}$	1.70		3.57	3.2		8.3
10128.770	$b\ ^4P_{1/2} - a\ ^4F_{3/2}$	5.82		7.84	13.6		18.3

As discussed earlier, the combined contributions of collisional excitation and fluorescence lead to complex temperature and density dependence in the relative strengths of dipole to forbidden emission lines. None the less, such ratios are much more sensitive to the strength of the dilution factor than to other parameters, so they can be used to diagnose the value of the dilution factor.

In Fig. 5, we plot Ti II line ratios between dipole-allowed and forbidden lines against the dilution factor, together with the observed ratios. These line ratios are very sensitive to the value of the dilution factor, but depend relatively little on T_e and N_e. From this figure, the line ratios for the nov01 observation are consistent with $\log_{10} w$ between -10.0 and -8.6, while the ratios from the mar00 spectrum indicate a higher dilution factor, by as much as 0.5 dex. These results are in agreement with those obtained with the [Ni II] lines.

Considering all possible line ratios among forbidden lines, we found one that is primarily sensitive to the dilution factor, and depends little on the temperature and density. This ratio is shown in Fig. 6, as computed for $T_e = 5000$, 6000 and 7000 K and $N_e = 10^6$, 10^7 and 10^8 cm^{-3}. Once again, the observed line ratios lay in the range of $\log_{10} w$ between -9.1 and -8.6.

From the agreement between various Ni II and Ti II diagnostics, we find the value of the dilution factor to be $\log_{10} w = -9.0 \pm 0.5$. With the dilution factor constrained, one can diagnose other parameters of the emitting region. Fig. 7 presents line ratios among Ti II forbidden lines versus the electron temperature. The line ratios are shown in various panels for $N_e = 10^6$, 10^7 and 10^8 cm^{-3}. In each case, we show the line ratios for $\log_{10} w = -9.0$, -8.5 and -9.5. The observed line ratios from the nov01 spectrum are also indicated. Inspection of these plot reveals that the best agreement for all the lines observed is obtained for $T_e = 6000 \pm 1000$ K.

This relatively low temperature is consistent with the observed ionization structure of Fe and Ni in the filament. The observed iron emission arises mostly from neutral iron, indicating that this dominates over Fe II. Because of the iron shielding of the filament, it is expected that there would be few photons capable of ionizing Fe I. But, even in the absence of photoionization collisional ionization drives most of the iron into Fe II whenever electron temperatures

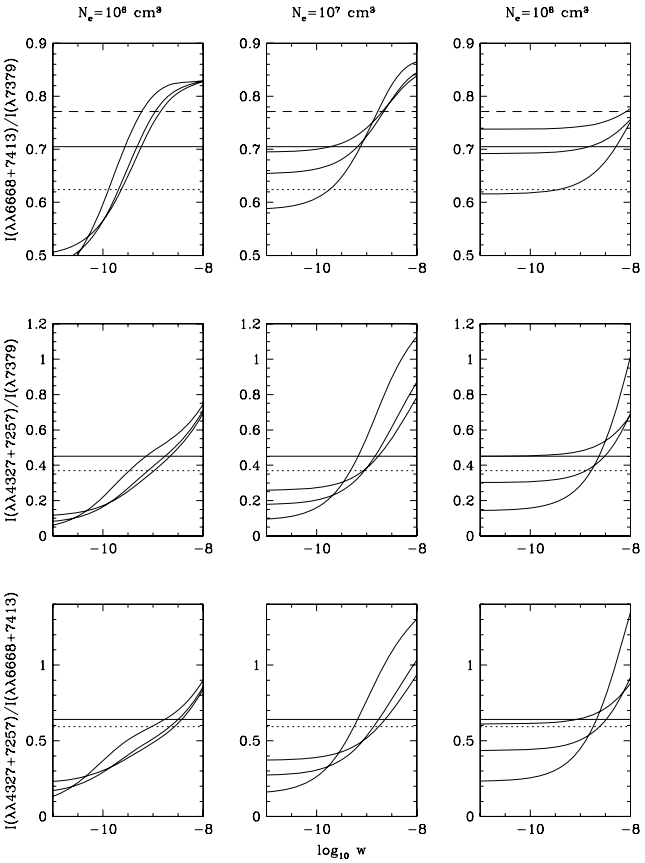

Figure 4. [Ni II] emissivity line ratios $I([\lambda\lambda 6668 + 7413])/I([\lambda 7379])$, $I([\lambda\lambda 4327 + 7257])/I([\lambda 7379])$ and $I([\lambda\lambda 4327 + 7257])/I([\lambda\lambda 6668 + 7413])$ against the logarithm of the dilution factor. The line ratios computed at $N_e = 10^6$, 10^7 and 10^8 cm^{-3} are presented in separate panels located from left to right. For each value of N_e, the line ratios are computed for temperatures of 5000, 7000 and 9000 K. The observed line ratios are indicted by horizontal lines as dashed line: mar00; dotted line: apr01 and solid line: nov01.

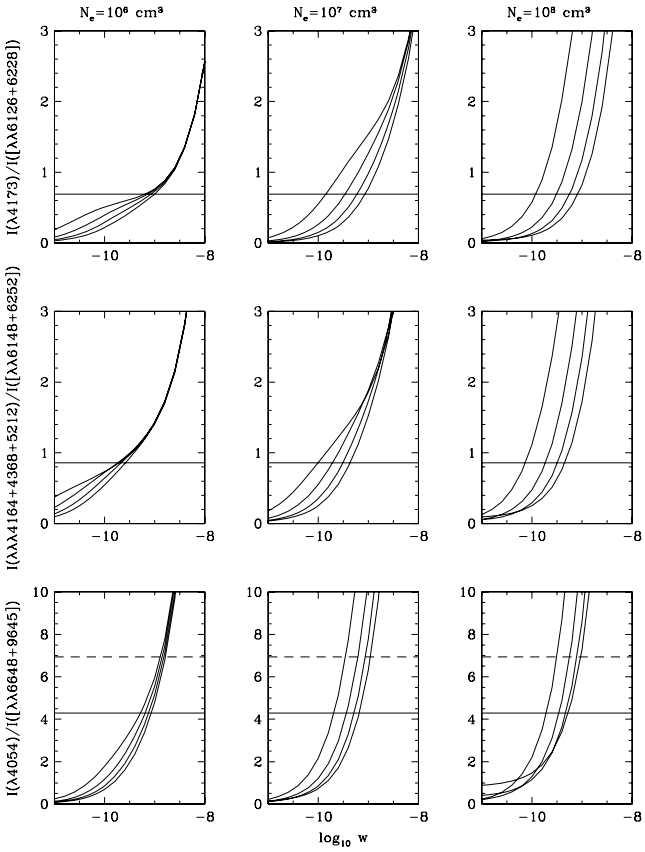

Figure 5. Ti II line ratios between dipole-allowed and forbidden line against the logarithm of the dilution factor. The line ratios computed at $N_e = 10^6$, 10^7 and 10^8 cm^{-3} are presented in separate panels located from left to right. For each value of N_e, the line ratios are computed for temperatures of 4000, 5000, 6000 and 7000 K. The observed line ratios for each observation are indicted by horizontal lines as dashed line: mar00 and solid line: nov01.

exceed ∼7000 K (see Arnaud & Raymond 1992). Below this temperature, neutral iron may be the dominant ionization stage. On the other hand, under collisional ionization conditions the fraction of ionized to neutral nickel is more than twice the fraction for iron at the same temperature. Thus, Ni II is expected to remain the dominant ionization stage for temperatures as low as ∼5000 K.

Finally, we can determine the electron density. Fig. 8 depicts four line ratios as function of the electron density for a fixed $\log_{10} w = -9.0$ and temperatures of 6000 ± 1000 K. The electron density is readily diagnosed at around 10^7 cm^{-3}.

Given the physical conditions diagnosed above, we compare the overall agreement between the computed spectrum and observations. This comparison for the nov01 spectrum is shown in Table 7. The agreement is reasonably good considering the remaining uncertainties in the atomic data and the shape of the pumping radiation continuum.

3.4 Spatial variations of the dilution factor

The Ti II $I([\lambda\lambda 6652 + 6727])/I([\lambda 4918])$ ratio is large across most of the spectral slit, which allows us to further investigate the spatial variations of the dilution factor near the Sr-filament. To do this, we integrated the intensity over 0.13 arcsec wide regions of the spectrum from mar00 and nov01. The measured line ratios, corrected for extinction, and the derived dilution factors from them are shown in Fig. 9. The mar00 observations, when the F2 fiducial (0.85 arcsec long) was centred on η Carinae with the large aperture extending radially from the star at the middle of the filament (1.3 arcsec from η Carinae), clearly show a linear decay of the dilution factor with distance from the central source. Consistently, with this picture, the nov01 slit that was centred on the Sr-filament and perpendicular to the radial direction from the central source shows a maximum of the dilution factor at the middle of the filament and symmetric drop-offs towards both sides of this position.

4 THE TITANIUM AND NICKEL ABUNDANCES IN THE SR-FILAMENT

Once the physical conditions of the Sr-filament have been determined, we proceed to compute the relative abundances of Ni II and Ti II. We use the nov01 spectrum because (i) much more spectral interval was covered during that visit and that greatly increased the number of lines, which permits a better statistical determination, and (ii) the long aperture likely sampled similar regions for the Ni II and Ti II due to the tangential slit orientation. None the less, we have confirmed that the computed relative abundances from all other observations also agree, within the uncertainties.

Fig. 10 depicts the N(Ti II)/N(Ni II) as derived from the [Ti II] λ6648 and [Ni II] λ7379 lines. The calculated abundance ratio is

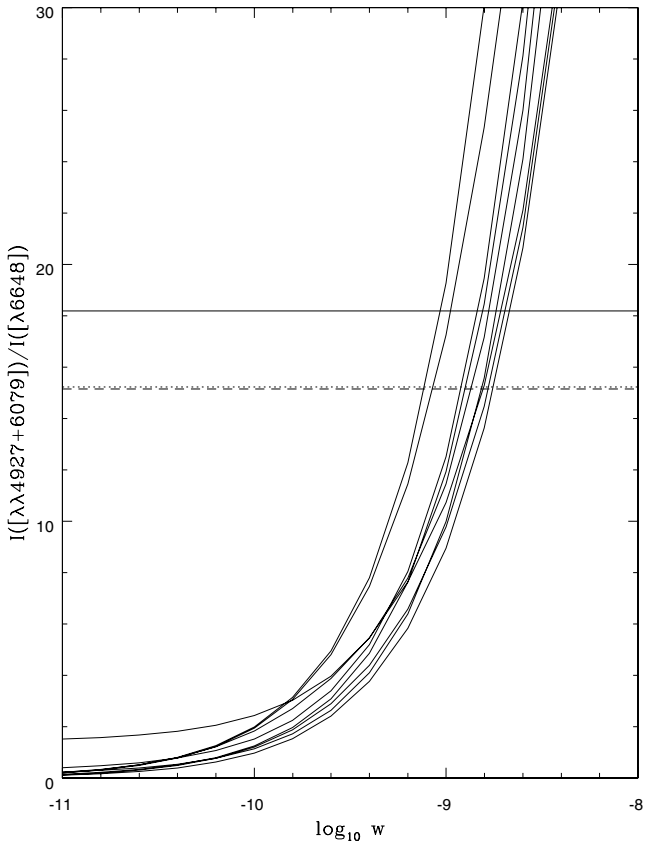

Figure 6. Ti II line ratios between forbidden lines, $I([\lambda\lambda 4927 + 6079])/I([\lambda 6648])$, against the logarithm of the dilution factor. The line ratios computed at $T_e = 4000$, 5000, 6000 and 7000 K and $N_e = 10^6$, 10^7 and 10^8 cm^{-3}. The observed line ratios for each observation are indicted by horizontal lines as dashed line: mar00; dotted line: apr01 and solid line: nov01.

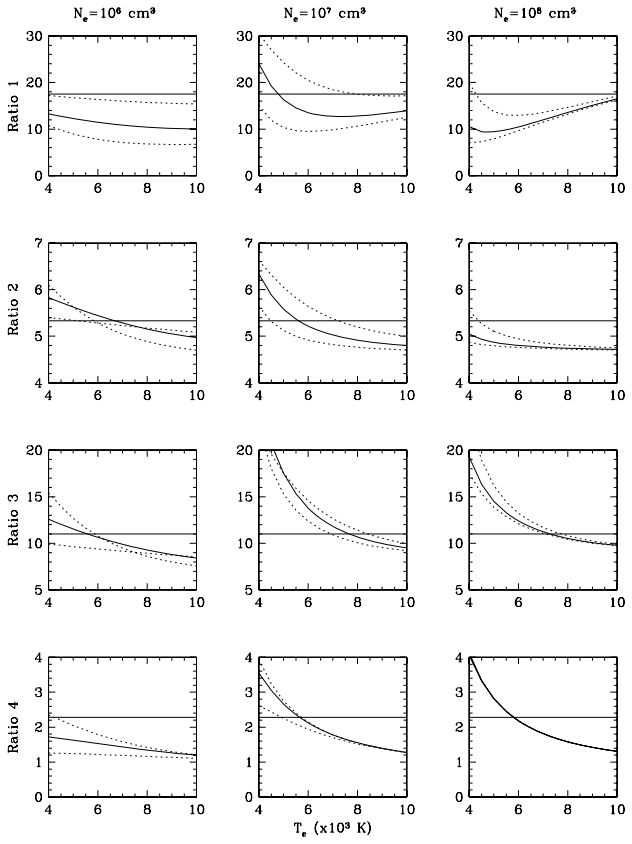

Figure 7. Ti II line ratios between forbidden lines versus T_e. The line ratios are $I([\lambda\lambda 6148 + 6252])/I([\lambda 6648])$ (Ratio 1), $I([\lambda\lambda 6652 + 6727])/I([\lambda 6648])$ (Ratio 2), $I([\lambda\lambda 7918 + 7977 + 8532 + 8587])/I([\lambda 6648])$ (Ratio 3) and $I([\lambda 10069b])/I([\lambda 6648])$ (Ratio 4). The line ratios computed for $N_e = 10^6$, 10^7 and 10^8 cm^{-3} are displayed in separated panels from left to right. In each case, $\log_{10} w = -9.0$ is indicated by the solid line and $\log_{10} w = -8.5$ and -9.5 are indicated by dotted lines. The observed line ratios for the nov01 are marked with horizontal lines.

plotted against the assumed value for the dilution factor and for temperatures of 6000 ± 1000 K as diagnosed from the spectrum. Given the fact that the lines observed from both species have similar excitation energies and arise from levels with the same multiplicity and parity, they respond similarly to changes in the dilution factor. So, we see that the uncertainty in the abundance ratio is negligible for the mean temperature of 6000 K, and uncertainty in the derived abundance does not exceed 20 per cent within the whole range of dilution parameters and temperatures. Thus, we conclude that N(Ti II)/N(Ni II) ≈ 2, with a conservative uncertainty that may not exceed a factor of 3, including the dispersion from all the lines which contains non-systematic uncertainties in the atomic data and the treatment of the pumping continuum field.

To estimate the total N(Ti)/N(Ni) abundance ratio, we note that only neutral and singly ionized ions are present in the spectra. It is expected that the ionic ratios Ti I/Ti II and Ni I/Ni II are similar since Ti I and Ni I have approximately the same ionization potential. Moreover, from observations one can conclude that Ni and Ti are both singly ionized, as there are no lines from the neutral stages of these ions in the spectra. Thus, N(Ti)/N(Ni) ≈ N(Ti$^+$)/N(Ni$^+$) ≈ 2 in gas phase. This value is significantly higher than the best solar abundance ratio of ∼0.05. In other words, the gas phase N(Ti)/N(Ni) abundance ratio in the Sr-filament is nearly two orders of magnitude greater than solar value.

Further, we have checked on the N(Ni II)/N(Fe II) abundance ratio in the filament. This calculation is complicated by the fact that the [Fe II] emission comes from a more extended region in velocity space. Thus, we only consider the integrated flux of [Fe II] lines within the range in velocity space that coincides with the [Ni II] emission. We find a value for the N(Ni II)/N(Fe II) ratio roughly consistent with the solar N(Ni)/N(Fe) ratio, assuming that the ionic fractions of Ni II and Fe II are tied to each other by charge exchange and are thus within a factor of 2 of each other. It must be noted, however, that the filament exhibits prominent emission from Fe I, suggesting a large abundance of this ion, but no emission from Ni I or Ti I within the sensitivity of the observations.

5 TITANIUM, NICKEL AND IRON CONDENSATION IN η CARINAE

The observed large overabundance of titanium with respect to both nickel and iron in the gas phase is quite striking. Ti/Fe abundance ratios higher than solar by up to 0.4 dex are known to occur in metal-poor and extremely metal-poor stars (Ryan, Norris & Beers 1996), but to the best of our knowledge there are no reports of such a high overabundance as we have analysed here. It is likely that the abnormal relative abundances found here are only representative of the gas phase, rather than the total absolute abundances. Under the

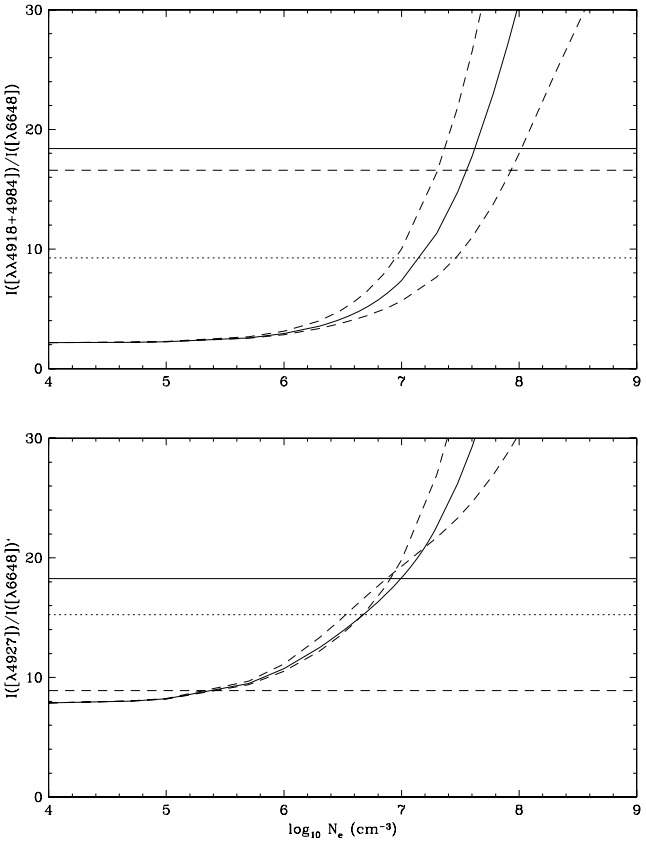

Figure 8. Ti II line ratios between forbidden lines versus N_e. The line ratios are computed for $T_e = 6000$ K (solid line), and $T_e = 5000$ K and $T_e = 7000$ K (dashed lines). The dilution factor was fixed in $\log_{10} w = -9.0$. The observed line ratios are indicted by horizontal lines as dashed line: mar00; dotted line: apr01 and solid line: nov01.

Table 7. Comparison between observed and theoretical line intensities for the nov01 spectrum. Line intensities are relative to $I([\lambda 6648]$. The theoretical spectrum was computed for $\log_{10} = -9.0$, $T_e = 6000$ K and $N_e = 10^7$ cm^{-3}.

λ	$I(\lambda)/I([\lambda 6648])$	
	Obs.	Theo.
4918.26	15.7	6.38
4927.29	18.2	18.3
4984.20	2.6	1.01
6079.57	2.4	0.91
6126.31	9.7	7.23
6148.90	2.6	1.78
6153.62	3.1	0.25
6228.99	1.6	0.91
6252.34	14.9	11.70
6648.98	1.0	1.0
6652.61	1.6	1.49
6727.67	3.7	3.72
7918.45	1.3	0.51
7977.90	2.9	0.84
8335.59	1.6	0.80
8412.35	3.3	2.46
8527.00	5.7	4.50
8531.91	4.5	4.39
8568.40	2.6	8.98
8587.49	2.4	8.04
9645.09	0.2	0.98
9652.72	0.5	0.74
10069 b	2.2	2.12
10128.77	2.7	3.26

conditions of the Sr-filament, nearly 90 per cent of Fe and Ni are condensed into grains. Thus, a large Ti/Ni gas phase abundance ratio would be attained if some kind of destruction mechanism of Ti-bearing condensates acted in the filament. Although we do not have a clear explanation for such a mechanism, we devote this section of the paper to study the chemistry of the Ti, Ni and Fe under the conditions of the Sr-filament.

Condensation temperatures of Ti, Fe and Ni are somewhat different, and Ti is generally more refractory than Fe and Ni during condensation from a solar composition gas (e.g. Lodders 2003). As described below, Ti also forms a more refractory condensate than Fe and Ni from the overall composition relevant for the ejecta here. Condensation temperatures depend on bulk composition and total pressure. In a solar composition gas with C/O = 0.5, titanium condenses as calcium titanate (e.g. perovskite, $CaTiO_3$), followed by an iron and nickel metal alloy at somewhat lower temperatures (Lodders 2003). Trace elements such as Sr condense into solid solution with major element host phases, and condensation of Sr as 'Sr-TiO_3' into $CaTiO_3$ proceeds at temperatures between that of $CaTiO_3$ and metal alloy formation. As long as the overall composition of η Carinae's ejecta remained near-solar, solar-type condensates should also have formed. However, in the Sr-filament, and in the rest of the emission ejecta within the Homunculus, the Little Homunculus and the Weigelt Blobs, very little oxygen has ever been detected. Moreover, in the Weigelt Blobs where [O I] λ6300 emission is seen, oxygen seems to be underabundant by at least two orders of magnitude (e.g. Thackeray 1967; Zethson 2001; Verner et al. 2005). In the outer ejecta, carbon and oxygen are severely depleted relative to solar abundances (Davidson et al. 1982; Dufour et al. 1997; Smith & Morse 2004). Hydrogen is also depleted whereas N and He are enriched. In order to explore the condensation chemistry, we adopt a solar composition gas in which solar C and O abundances are both reduced by a factor of 100. The N abundance is increased by the amount removed from the solar C and O abundances so that the sum of solar CNO nuclei is preserved. The He abundance is taken as solar plus a quarter of the solar H abundance, and the H abundance is set to zero. Note that the chemistry of Ti, Fe, Ni and Si is relatively insensitive to the total H abundance because there are no major H-bearing gases for those elements. Even if H were fairly abundant, the following condensation results would change little. Descriptions of the thermochemical computation methods are given in Lodders (2003) and Lodders & Fegley (1997). The results of this calculation serve as a good illustration of the dust chemistry, and should remain qualitatively correct despite variations of the precise relative abundances. The condensates (Fig. 11) for this 'CNO'-processed composition are first TiC, and at about 100 K lower temperature, an iron–nickel silicide alloy, (Fe,Ni)Si. Below total pressures of $\sim 10^{-7}$ bar, SiC condensation temperatures are within a few degrees of those of the silicide alloy.

The condensates from the 'CNO'-processed composition are the same as appear when C and O abundances of an otherwise solar composition gas are only slightly (i.e. of the orders of the factor of 2) modified so that C/O $\geqslant 1$ (Lodders & Fegley 1995, 1999). Here, the C/O ratio remains solar but the large decrease in absolute C and O abundances is responsible for the appearance of the carbides and

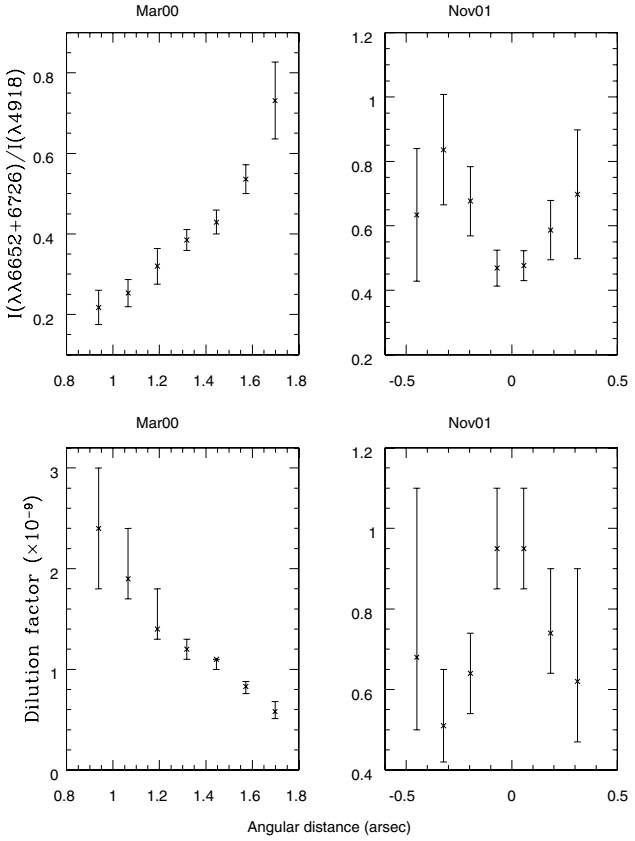

Figure 9. [Ti II] flux line ratios, $I(\lambda\lambda 6652 + 6727)/I(\lambda 4918)$ (upper plots) and derived dilution factors (lower plots) against the angular distance along the spectral slits of mar00 (radial across the filament from the central source) and nov01 (tangential across the filament).

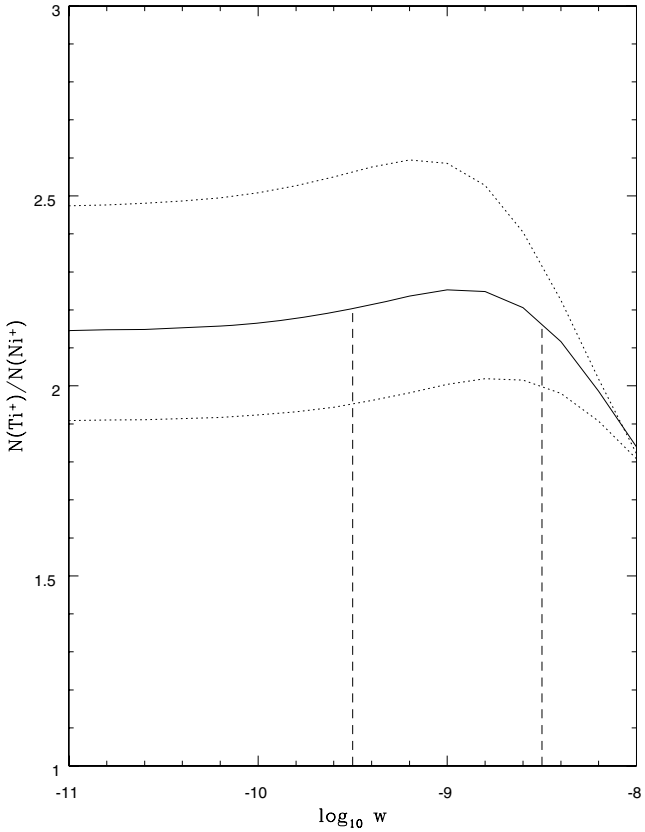

Figure 10. $N(Ti^+)/N(Ni^+)$ abundance ratio from the spectrum of the Sr-filament as obtained for any given dilution factor between 10^{-11} and 10^{-9}. The solid line depicts the abundance ratios for an adopted temperature of 6000 K, while the results for temperatures of 5000 and 7000 K are indicated by the dotted lines. The vertical dashed lines indicate the range of the dilution factor as diagnosed from the spectrum.

silicide because there is no oxygen for SiO and silicate or oxide formation.

The elemental composition here has enough C for condensation of all Ti as TiC (the total Ti/C is ∼0.03) but only a little SiC can form because Si is more abundant than C (Si/C ∼ 14) and Si condenses also into (Fe,Ni)Si. The overall C abundance is so low that graphite does not condense at the relatively high temperatures where TiC and (Fe, Ni)Si form. If carbon were completely absent here, titanium nitride (TiN, osbornite) would condense instead of TiC at about the same temperature, SiC would be completely absent and condensation of (Fe, Ni)Si would remain unchanged.

Condensation temperatures describe when a compound starts to form (i.e. where the saturation ratio reaches unity), but lower temperatures are needed to fully remove an element from the gas into a condensate, as shown for a constant total pressure in Fig. 12. Complete titanium removal from the gas requires a drop of about 100 K below the condensation temperature of TiC, and all Ti is condensed at temperatures when (Fe, Ni)Si condensation begins to proceed.

Given the nature of the Ti-, Ni- and Fe-bearings described here, we suggest that selective photoevaporation of Ti-bearings is a possible explanation for the gas phase Ti/Ni abundance found in the filament. Two different scenarios may be suggested: (i) there was some spatial separation between the TiC and (Ni,Fe)Si condensates, related to their different condensation temperatures, that left the TiC-rich gas more exposed to photoevaporation; (ii) the TiC grains are generally smaller than the (Ni,Fe)Si grains, and so the TiC condensates were much less resistant to photoevaporation.

These scenarios sketched out here seem promising to explain the observations and need to be studied in more detail. Further, it is important to determine the abundance ratios of other elements of different volatility.

6 SUMMARY AND CONCLUSIONS

We have studied the Ni II and Ti II spectra of the Sr-filament in η Carinae, as taken in three different epochs with the *HST*. In doing this, we build spectral models for the two ions using the best published data for Ni II, while we carry out extensive calculations of radiative and electron impact rates for Ti II.

The spectral models were employed for diagnosing the physical conditions of the emitting region. The results are generally consistent with previous determinations using [Sr II] and Sr II lines. Moreover, the [Ti II] lines allow us to constrain the conditions for observations with the aperture across the η Carinae's central source to $N_e \approx 10^7$ cm^{-3}, $T_e = 6000 \pm 1000$ K and dilution factor $\log_{10} w = -9.0 \pm 0.5$ for an assumed blackbody continuum radiation with temperature of 35 000 K. For observations with the slit perpendicular to the radial direction, the dilution factor seems to be somewhat lower.

Study of the observed [Ti II] emission reveals a very large overabundance of Ti in gas phase with respect to Ni and Fe relative to the cosmic values.

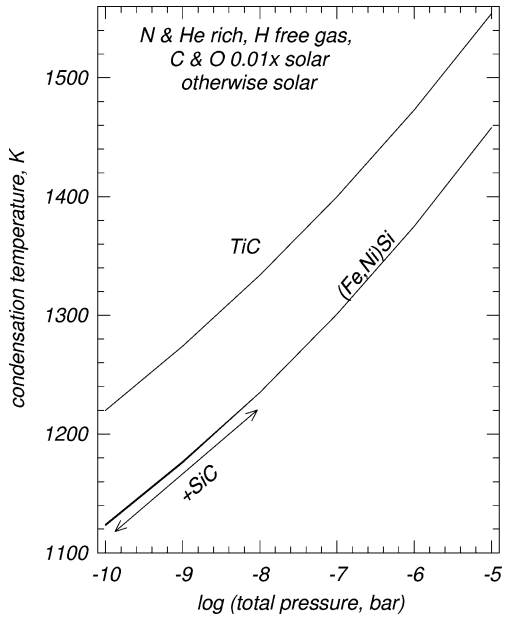

Figure 11. Condensation temperatures as a function of total pressure.

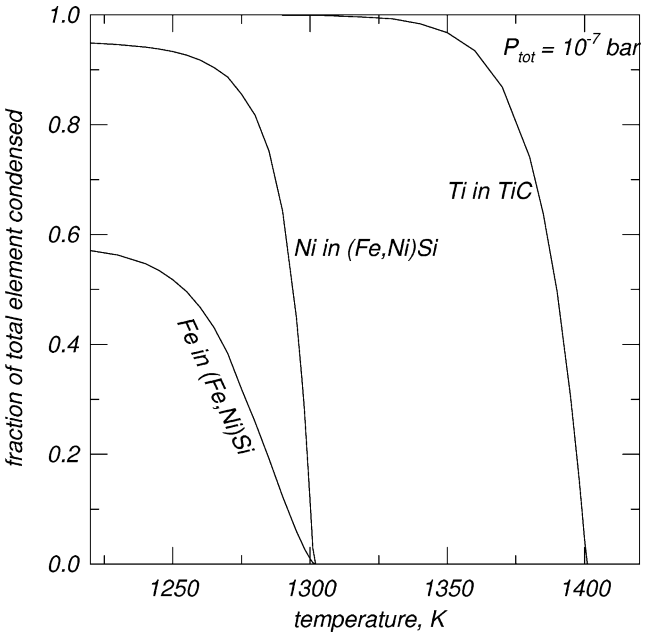

Figure 12. The fraction of an element condensed as a function of temperature at a constant total pressure of 10^{-7} bar.

We study the chemistry of Ti, Ni and Fe in CNO-cycled gas and find that Ti condenses as TiC, or alternatively as TiN, while Ni and Fe are locked into (Ni,Fe)Si. Moreover, the TiC condenses at higher temperatures than Ni- and Fe-bearings. Later, we suggest that the TiC would be selectively destroyed by the stellar UV radiation leading to a relative overabundance of Ti in gas phase.

This explanation for the unusual Ti/Ni ratios in the Sr-filament requires that significant dust and molecules had formed in this material shortly after the Great Eruption, but have since been largely photoevporated here. In this context, it is very interesting that near-IR emission from molecular hydrogen is seen throughout the polar lobes of the Homunculus Nebula (Smith 2002a), but this same H_2 emission is not seen at comparable levels from the equatorial skirt in the vicinity of the Sr-filament (Smith 2002a, 2004). Today, the gas densities we infer in the Sr-filament ($\sim 10^7$ cm^{-3}) are very high compared to many other circumstellar nebulae around massive stars, and are similar to the extremely high densities seen in the walls of the Homunculus (e.g. Gull et al. 2005; Nielsen, Gull & Vieira-Kober 2005). A weaker radiation field at larger radii is not the only explanation for this difference: H_2 emission is seen both in the polar caps of the Homunculus at larger radii from the star than the Sr-filament and in the side walls of the polar lobes near the equator, even *closer* to the star than the Sr-filament (Smith 2004). In the past when the Sr-filament ejecta were even denser, it is conceivable that H_2 or other molecules may have existed, but have since been destroyed. If true, this would seem to support the scenario of unusual chemistry resulting from selective photoevaporation and CNO-processed ejecta, as we have suggested here.

ACKNOWLEDGMENTS

The observations of the strontium filament were made with the STIS on the NASA/ESA *HST* and were obtained by the Space Telescope Science Institute, which is operated by the Association of Universities for Research in Astronomy, Incorporated, under NASA contract NAS5-26555. Support for this research was provided in part by NASA through the STIS GTO grant and grants from the Space Telescope Science Institute. HH is supported by a grant from the Swedish National Space Board. NS was supported by NASA through grant HF-01166.01A from STScI. Work by KL was supported in part by grant NNG04G157A from the NASA Astrobiology Institute. Data for this analysis were gathered under GO programs headed by Kris Davidson and GO and GTO programs headed by Theodore Gull.

We thank Sveneric Johansson for much guidance and advice.

REFERENCES

Arnaud M., Raymond J., 1992, ApJ, 398, 394
Badnell N. R., 1986, J. Phys. B, 19, 3827
Bautista M. A., 2004, A&A, 420, 763
Bautista M. A., Gull T. R., Ishibashi K., Hartman H., Davidson K., 2002, MNRAS, 331, 875
Bautista M. A., Peng J., Pradhan A. K., 1996, ApJ, 460, 372
Berrington K. A., Burke P. G., Eissner W., Norrington P. N., 1995, Comput. Phys. Commun., 92, 290
Bizzarri A., Huber M. C. E., Noels A., Grevesse N., Bergeson S. D., Tsekeris P., Lawler J. E., 1993, A&A, 273, 707
Blackwell D. E., Menon S. L. R., Petford A. D., 1982, MNRAS, 201, 603
Burgess A., 1974, J. Phys. B: At. Mol. Phys., 7, L364
Cardelli J. A., Clayton G. C., Mathis J. S., 1989, ApJ, 345, 245
Damineli A., 1996, ApJ, 460, L49
Danzmann K., Kock M., 1980, J. Phys. B: Atom. Mol. Op. Phys., 13, 2051
Davidson K., Humphreys R. M., 1997, ARA&A, 35, 1
Davidson K., Walborn N. R., Gull T. R., 1982, ApJ, 254, 47
Davidson K., Dufour R. J., Walborn N. R., Gull T. R., 1986, ApJ, 305, 867
Davidson K., Smith N., Gull T. R., Ishibashi K., Hillier D. J., 2001, AJ, 121, 1569
Dufour R. J., Glover T. W., Hester J. J., Currie D. G., van Orsow D., Walter D. K., 1997, ASP Conf. Ser. Vol. 120, Astron. Soc. Pac., San Francisco, p. 255
Eissner W., Nussbaumer H., 1969, J. Phys. B, 2, 1028
Eissner W., Jones M., Nussbaumer H., 1974, Comput. Phys. Commun., 8, 270
Gaviola E., 1950, ApJ, 111, 408
Gull T. R., Vieira G., Bruhweiler F., Nielsen K. E., Verner E., Danks A., 2005, ApJ, 620, 442

Hartman H. et al., 2003, J. Phys. B: Atom. Mol. Op. Phys., 36, L197
Hartman H., Gull T., Johansson S., Smith N., *HST* Eta Carinae Treasury Project Team, 2004, A&A, 419, 215
Hartman H. et al., 2005, MNRAS, 361, 206
Huldt S., Johansson S., Litzen U., Wyart J. F., 1982, Phys. Scr., 25, 401
Hummer D. G., Berrington K. A., Eissner W., Pradhan A. K., Saraph H. E., Tully J. A., 1993, A&A, 279, 298
Ishibashi K. et al., 2003, AJ, 125, 3222
Kurucz R. L., 2000, http://kurucz.harvard.edu/
Lodders K., 2003, ApJ, 591, 1220
Lodders K., Fegley B., 1995, Meteoritics, 30, 661
Lodders K., Fegley B., 1997, in Bernatowicz T., Zinner E., eds, AIP Conf. Proc. 402, The Astrophysical Implications of the Laboratory Study of Presolar Materials. Am. Inst. Phys., Woodbury, NY, p. 391
Lodders K., Fegley B., 1999, in LeBertre T., Lebre A., Waelkens C., eds, Proc. IAU Symp. 191, Asymptotic Giant Branch Stars. Astron. Soc. Pac., San Francisco, p. 279
Meggers I. W. F., Corliss C. H., Scribner B. F., 1975, NBS Mono. 145, Washington, DC
Moore C. E., 1949, Atomic Energy Levels, Natl. Bur. Stand. (US) Circ. 467, Vol. I [reissued in 1971 as Natl. Bur. Stand. (US) Natl. Stand. Ref. Data Ser. 35, Vol. I]
Morse J. A., Kellogg J. R., Bally J., Davidson K., Balick B., Ebbets D., 2001, ApJ, 548, L207
Nielsen K. E., Gull T. R., Vieira-Kober G., 2005, ApJS, 157, 138
NIST, 2000, http://www.nist.gov/cgi-bin/AtData/main_asd
Pickering J. C., Thorne A. P., Perez R., 2001, ApJS, 132, 403
Pickering J. C., Thorne A. P., Perez R., 2002, ApJS, 138, 247
Roberts I. J. R., Andersen T., Sorensen G., 1973, ApJ, 181, 567
Roberts I. J. R., Voigt P. A., Czernichowski A., 1975, ApJ, 197, 791
Russell H. N., 1927, ApJ, 66, 283
Ryan S. G., Norris J. E., Beers T. C., 1996, ApJ, 471, 254
Smith N., 2002a, MNRAS, 337, 1252
Smith N., 2002b, MNRAS, 331, 7
Smith N., 2004, MNRAS, 351, L15
Smith N., 2005, MNRAS, 357, 1330
Smith N., Gehrz R. D., 1998, AJ, 116, 823
Smith N., Morse J. A., 2004, ApJ, 605, 854
Smith N., Gehrz R. D., Hinz P. M., Hoffmann W. F., Hora J. L., Mamajek E. E., Meyer M. R., 2003, AJ, 125, 1458
Smith N. et al., 2004, ApJ, 605, 405
Tapia M., Roth M., Vázquez R. A., Feinstein A., 2003, MNRAS, 339, 44
Thackeray A. D., 1967, MNRAS, 135, 51
Verner E., Bruthweiler F., Gull T., 2005, ApJ, 624, 973
Weigelt G. et al., 1995, in Niemala V., Morrell N., Feinstein A., eds, Rev. Mex. Astron. Astrofis. Ser. Conf., Vol. 2, The Eta Carinae Region: A Laboratory of Stellar Evolution. UNAM, Mexico, p. 11
Zethson T., 2001, PhD thesis, Lund Univ.
Zethson T., Gull T. R., Hartman H., Johansson S., Davidson K., Ishibashi K., 2001, AJ, 122, 322

This paper has been typeset from a TEX/LATEX file prepared by the author.